

AN UPPER GRAVITY-WAVE ABSORBING LAYER FOR NWP APPLICATIONS

J. B. Klemp and J. Dudhia

National Center for Atmospheric Research  
Boulder, Colorado

A. D. Hassiotis

The Pennsylvania State University  
State College, Pennsylvania

ABSTRACT

Although the use of a damping layer near the top of a computational model domain has proven effective in absorbing upward-propagating gravity-wave energy in idealized simulations, this technique has been less successful in real atmospheric applications. Here, a new technique is proposed for nonhydrostatic model equations that are solved using split-explicit time integration techniques. In this method, an implicit Rayleigh damping term is applied only to the vertical velocity, as a final adjustment at the end of each small (acoustic) time step. The adjustment is equivalent to including an implicit Rayleigh damping term in the vertical momentum equation together with an implicit vertical diffusion of  $w$ , and could be applied in this manner in other time integration schemes. This implicit damping for the vertical velocity is unconditionally stable and remains effective even for hydrostatic gravity waves. The good absorption characteristics of this layer across a wide range of horizontal scales are confirmed through analysis of the linear wave equation and numerical mountain-wave simulations, and through simulations of an idealized squall line and of mountain waves over the Colorado Rocky Mountains.

---

## 1. Introduction

While it is well known that internal gravity waves play an important role in the dynamics of mesoscale circulations, their treatment in numerical simulation models has been problematic. A major impediment to the accurate representation of gravity waves stems from artificial influences of the upper boundary in the model domain. Conventional upper boundary conditions, such as a rigid lid or constant pressure surface, are totally reflective to upward propagating gravity-wave energy. Although both gravity-wave radiation boundary conditions and upper absorbing layers have been developed, these techniques have, in practice, proven more successful in idealized research simulations than in real atmospheric NWP applications. In this paper, we propose a simple approach for implementing an upper absorbing layer in split-explicit models that may prove more effective in many mesoscale NWP applications.

One approach for reducing the artificial reflection of gravity-wave energy at the top of a model domain is to employ a gravity-wave radiation condition along the upper boundary. A radiation condition for linear gravity waves can be derived that is independent of both the wave frequency and vertical wavelength for hydrostatic waves in the absence of rotation (i. e. Klemp and Durran, 1983, Bougeault, 1983). The derivation of this radiation condition assumes that a layer of infinite depth exists above the top boundary of the model, in which the wind and stability is horizontally homogeneous and constant with height. While these restrictions may be acceptable for many applications involving idealized flow, they are not as well suited for the horizontal inhomogeneities and wide range of scales encountered in numerical weather prediction. Nevertheless, this radiation condition has been implemented and used productively in the Navy COAMPS Model (i.e. Jiang and Doyle, 2004, Doyle et al., 2005), and a localized version is available in the MM5 Model (Grell et al., 1995).

An alternative approach for mitigating gravity-wave energy reflection at the upper boundary is to include a damping (sponge) layer in the upper portion of the model domain. This layer may employ either horizontal diffusion or Rayleigh damping terms

---

*Corresponding author address:* Dr. Joseph B. Klemp, National Center for Atmospheric Research, P.O. Box 3000, Boulder, Colorado, 80307-3000; email: *klemp@ucar.edu*

with damping coefficients that increase with height over a depth sufficient to achieve good absorption characteristics (i.e. Klemp and Lilly, 1978, Durran and Klemp, 1983). Although a horizontal diffusion layer is conceptually well suited for both idealized and real-data simulations, for many practical applications, the maximum stable diffusion coefficient is significantly smaller than the values required to achieve effective absorption of gravity-wave energy. To illustrate this limitation, let's assume that the practical linear stability limit on the dimensionless second order diffusion coefficient is approximately  $K_H \Delta t / \Delta x^2 \simeq 0.1$  (including multi-dimensions and added limitations from other effects such as advection). At this limit,  $K_H k / U = 0.2\pi(\Delta x / \lambda_H) c_R^{-1}$ , where  $\lambda_H$  is the horizontal wavelength of gravity waves to be absorbed, and  $c_R = U \Delta t / \Delta x$  is the advective Courant number. For waves having  $\lambda_H = 6\Delta x$  and  $c_R = 0.2$ ,  $K_H k / U \simeq 0.5$ , which is considerably smaller than values ( $\sim 2$ ) required to prevent significant wave reflection for typical absorbing layer depths (see Klemp and Lilly, 1978, Fig.1). For better resolved waves or higher Courant numbers, the upper limit on this damping parameter gets even smaller. Hahn (2007) discusses difficulties in successfully applying a horizontal-diffusion absorbing layer in the WRF/ARW Model that are consistent with this stability limitation. Zängl (2007) has attempted to improve the effectiveness of a horizontal diffusion absorbing layer by altering the diffusion operator to produce relatively higher damping at larger horizontal scales. Including vertical diffusion in the damping layer can provide additional absorption of gravity wave energy (i.e. in the WRF/ARW Model, Skamarock et al., 2005, Zängl, 2007). However, vertical diffusion terms have similar linear stability constraints to horizontal diffusion and may also alter the vertical structure of the larger scale environment.

Although the implementation of an absorbing layer using Rayleigh damping can work well for idealized simulations with a known background environmental state, difficulties arise in NWP applications because the entire atmospheric state is evolving as part of the simulation. To address this complication, modelers have imposed Rayleigh damping layers in which fields are relaxed toward a larger scale representation of the atmosphere, achieved by Fourier filtering smaller horizontal scales (i.e. Chen et al., 2005) or other relaxation techniques [i.e. in the Meso-NH Model (Bougeault and Mascart, 2001), and the COAMPS Model (Jim Doyle, personal communication)], or using nudging techniques based on observations or other large-scale analyses [i.e. for the RAMS Model (MRC/Aster, 2000), and the MM5 Model (Wei et al., 2002)]. While these are more sophisticated techniques, they still require *a priori* decisions

as to which scales will be damped for particular applications.

Here, we present a new approach for a gravity-wave absorbing layer that is simple to implement in split-explicit time-integration schemes and appears to work well for both idealized and real-data (NWP) applications. With this approach, an implicit Rayleigh damping term for the vertical velocity is added as a final adjustment at the end of each small (acoustic) time step. In section 2, we describe the procedure for including the Rayleigh-damping term in the time-split integration for the nonhydrostatic equations expressed in height coordinates (including a corresponding description for the mass-coordinate equations in the Appendix). We then analyze the linear wave equation that includes this absorbing layer (section 3) to quantify the reflection characteristics as a function of horizontal scale as well as the depth and strength of the damping region. Numerical mountain-wave simulations are presented in section 4 to demonstrate quantitatively the effectiveness of this approach across a wide range of horizontal scales. We further illustrate the utility of our proposed absorbing layer in an idealized squall-line simulation (section 5) and in an NWP forecast for mountain waves over the eastern slope of the Colorado Rocky Mountains (section 6). Finally, in section 7, we summarize this technique and provide some guidance for specification of the Rayleigh damping coefficient.

## 2. An Implicit Rayleigh damping layer in the split-explicit numerical integration

For simplicity, we shall discuss our implementation of an upper gravity-wave absorbing layer in the context of the inviscid (except for the absorbing layer) dry nonhydrostatic equations in Cartesian  $(x, z)$  coordinates. Expressing the potential temperature  $\theta = \bar{\theta}(z) + \theta'$  and the Exner function  $\pi = \bar{\pi}(z) + \pi'$  as perturbations about a specified reference sounding, these equations can be written on an  $f$  plane without further approximation as:

$$\partial_t \mathbf{V}_H + c_p \theta \nabla_H \pi' = -\mathbf{V} \cdot \nabla \mathbf{V}_H - f \mathbf{k} \times \mathbf{V} \equiv \mathbf{F}_{V_H} \quad (1)$$

$$\partial_t w + c_p \theta \partial_z \pi' - g \frac{\theta'}{\bar{\theta}} = -\mathbf{V} \cdot \nabla w \equiv F_w \quad (2)$$

$$\partial_t \theta' + w \partial_z \theta = -\mathbf{V} \cdot \nabla_H \theta' \equiv F_\theta \quad (3)$$

$$\partial_t \pi' + C \nabla \cdot \rho \theta \mathbf{V} = 0 \quad (4)$$

where  $C = c^2 / (c_p \rho \theta^2)$  with  $c^2 = (c_p / c_v) RT$  being the square of the sound speed,  $\mathbf{V} = (u, v, w)$ , and the subscript  $H$  refers to the horizontal vector components.

In time-split integration schemes, terms on the left-hand sides of (1)-(4) are integrated forward in time over a series of small time intervals  $\Delta\tau$  while the the right-hand sides  $F(\ )$  are held fixed at time

*t.* We represent terms responsible for gravity waves and for horizontally propagating sound waves with forward-backward time differencing, and treat the vertical sound-wave propagation terms implicitly. To implement our proposed absorbing layer, we add an adjustment step to the small-time-step integration, which can be written in the form

$$\mathbf{V}_H^{\tau+\Delta\tau} = \mathbf{V}_H^\tau - \Delta\tau \left( c_p \theta^t \nabla_H \pi'^{\tau} - \mathbf{F}_{V_H}^t \right) \quad (5)$$

$$\pi'_1 = \pi'^{\tau} - \Delta\tau C^t \left[ \nabla \cdot \rho^t \theta^t \mathbf{V}_H^{\tau+\Delta\tau} + \frac{1}{2} \partial_z (\rho^t \theta^t w^\tau) \right] \quad (6)$$

$$w^{\tau*} = w^\tau - \Delta\tau \left( c_p \theta^t \overline{\partial_z \pi'^{\tau*}} - g \frac{\theta'^{\tau}}{\theta} - F_w^t \right) \quad (7)$$

$$\pi'^{\tau*} = \pi'_1 - \frac{1}{2} \Delta\tau C^t \partial_z (\rho^t \theta^t w^{\tau*}) \quad (8)$$

$$\boxed{w^{\tau+\Delta\tau} = w^{\tau*} - R_w \Delta\tau w^{\tau+\Delta\tau}} \quad (9)$$

$$\theta'^{\tau+\Delta\tau} = \theta'^{\tau} - \Delta\tau \left( w^{\tau+\Delta\tau} \partial_z \theta^t - F_\theta^t \right) \quad (10)$$

$$\pi'^{\tau+\Delta\tau} = \pi'_1 - \frac{1}{2} \Delta\tau C^t \partial_z (\rho^t \theta^t w^{\tau+\Delta\tau}), \quad (11)$$

where the overbar labeled  $\tau^*$  denotes an average of the variable at time  $\tau$  and its intermediate state  $\tau^*$ , and the boxed equation (9) represents the added adjustment in the form of an implicit Rayleigh damping on  $w$ .

In the traditional time-split integration, a small time step is computed in the order of the above equations [with  $\tau^* = \tau + \Delta\tau$  and with (9) omitted] :  $\mathbf{V}_H^{\tau+\Delta\tau}$  is obtained from (5);  $w^{\tau+\Delta\tau}$  is computed by solving a tridiagonal matrix for the vertically implicit equation produced by combining (7) and (8), using the known portion of the pressure equation  $\pi_1$  in (6); and finally,  $\theta'^{\tau+\Delta\tau}$  and  $\pi'^{\tau+\Delta\tau}$  are recovered from (10) and (11), respectively, knowing  $w^{\tau+\Delta\tau}$ . Our proposed Rayleigh-damping adjustment (9) on  $w$  is applied following the vertically implicit calculation of  $w$  [now represented in (7) and (8) as an intermediate value at  $\tau^*$  instead of what would have been the final value at  $\tau + \Delta\tau$  in the absence of (9)]. Thus, the addition of this damping adds only a single line of code to the small-time-step calculations.

Notice that the inclusion of this Rayleigh damping as an adjustment step is different from adding an implicit Rayleigh damping term directly in the  $w$  equation (7). This is demonstrated by combining (7)-(9) and (11) to eliminate  $w^{\tau*}$  and  $\pi'^{\tau*}$ , with the result:

$$\begin{aligned} \partial_\tau w + c_p \theta^t \partial_z \overline{\pi'^{\tau}} - g \frac{\theta'^{\tau}}{\theta} + R_w w^{\tau+\Delta\tau} \\ - \frac{1}{4} \Delta\tau^2 c_p \theta^t \partial_z \left[ C^t \partial_z (\rho^t \theta^t R_w w^{\tau+\Delta\tau}) \right] = F_w^t, \end{aligned} \quad (12)$$

$$\partial_\tau \pi' + C^t \left[ \nabla \cdot \rho^t \theta^t \mathbf{V}_H^{\tau+\Delta\tau} + \partial_z (\rho^t \theta^t \overline{w^\tau}) \right] = F_\pi^t, \quad (13)$$

where the overbar labeled  $\tau$  now denotes an average of the variable at time  $\tau$  and its final state at  $\tau + \Delta\tau$ . Here, there are two terms involving  $R_w$  in (12). The first is the same as a Rayleigh damping term added directly to the  $w$  equation. The second term containing  $R_w$ , however, appears because the Rayleigh damping is actually applied as an adjustment step (9). This term has the form of an implicit vertical diffusion of  $w$  and is multiplied by the square of the time step. As demonstrated in the next section, this second  $R_w$  term in (12) enables the absorption of vertically propagating gravity-wave energy even when the waves are essentially hydrostatic.

Adapting this technique in time-split nonhydrostatic NWP modeling systems should be straight forward without additional complications. For example, whether the model equations are cast in advective or flux form using either height or mass for the vertical coordinate, an adjustment comparable to (9) can be applied to the prognostic variable for vertical velocity immediately after its intermediate value has been calculated, and will produce similar absorption characteristics (demonstrated for the mass coordinate in the Appendix). Also, the gravity-wave terms [the buoyancy term in (7) and vertical advection term in (10)] can be treated implicitly without additional complication.

### 3. Analysis of implicit Rayleigh damping on $w$ for steady linear mountain waves

To demonstrate the behavior of this upper boundary implicit Rayleigh damping layer, we follow the approach of Klemp and Lilly (1978) and evaluate the reflection characteristics for vertically propagating inertia-gravity waves for steady-state flow over terrain. For this analysis, we consider the 2-D linearized form of (1)-(4) with the additional simplifications that  $U^2 \ll c^2$  and the vertical wavelength  $\lambda_z \ll 4\pi H_\rho$ , where  $H_\rho$  is the density scale height, which are good approximations for this analysis. The steady-state linear representation of equations (5), (10), (12), and (13) for a constant mean wind  $U$  and stability  $N$  then becomes

$$U \partial_x u' + \partial_x p' - f v' = 0 \quad (14)$$

$$U \partial_x v' + f u' = 0 \quad (15)$$

$$\begin{aligned} U \partial_x w + \partial_z p' - b' + R_w w \\ - \frac{1}{4} c^2 \Delta\tau^2 \partial_{zz} (R_w w) = 0 \end{aligned} \quad (16)$$

$$U \partial_x b' + N^2 w = 0 \quad (17)$$

$$\partial_x u + \partial_z w = 0, \quad (18)$$

where  $p' = c_p \bar{\theta} \pi'$ ,  $b' = g \theta' / \bar{\theta}$ , and  $N^2 = g \bar{\theta}_z / \bar{\theta}$ . Representing the dependent variables  $\psi$  in terms of

their Fourier components  $\psi(x, z) = \hat{\psi}(z) \exp(ikx)$ , (14)-(18) can be combined into a single wave equation

$$\partial_{\tilde{z}\tilde{z}} \left[ (1 - F^2 - i\frac{1}{4}\alpha^2\beta_w)\hat{w} \right] + \left[ 1 - K^2(1 - i\beta_w) \right] \hat{w} = 0. \quad (19)$$

Here, the coefficients are expressed dimensionless form:

$$K = \frac{kU}{N}, \quad F = \frac{f}{kU}, \quad \alpha = kc\Delta\tau, \quad \beta_w = \frac{R_w}{kU}, \quad (20)$$

and the dimensionless vertical coordinate  $\tilde{z} = Nz/U$  is scaled by the vertical wavenumber for hydrostatic nonrotating waves. Notice that although for simplicity we have cast this analysis in terms of steady mountain waves, the same analysis holds for propagating gravity waves if we just replace the mean wind speed  $U$  with the phase speed  $U \pm c_H$ , where  $c_H = \omega/k$  is the intrinsic horizontal phase speed of the wave.

To evaluate the reflection characteristics of the upper absorbing layer, we solve (19) for a specified profile of  $\beta_w(\tilde{z})$  between the bottom of the layer at  $\tilde{z}_d$  and the top of the model domain at  $\tilde{z}_t$ . Here, we adopt the damping profile proposed by Klemp and Lilly (1978):

$$\beta_w(\tilde{z}) = \beta_{max} \sin^2 \left( \frac{\pi}{2} \frac{\tilde{z} - \tilde{z}_d}{\tilde{z}_t - \tilde{z}_d} \right). \quad (21)$$

Beneath the absorbing layer, the inviscid solution ( $\beta_w = 0$ ) for a single wave number  $k$  has the form

$$\hat{w}_l(\tilde{z}) = C_1 e^{i\Lambda_z(\tilde{z} - \tilde{z}_d)} + C_2 e^{-i\Lambda_z(\tilde{z} - \tilde{z}_d)}, \quad (22)$$

where  $\Lambda_z = [(1 - K^2)/(1 - F^2)]^{\frac{1}{2}} = N\lambda_z/U$  is the dimensionless vertical wavenumber. For  $\Lambda_z^2 > 0$  and  $k > 0$ , the first term on the right hand side of (22) corresponds to the mode with upward-propagating wave energy, while the second term represents the downward-propagating mode. Thus, the ratio  $r = |C_2/C_1|$  is a measure of the wave reflection that occurs in the absorbing layer above this inviscid region.

To match the solution of (19) in the absorbing layer to the inviscid solution (22) below, we require the pressure and vertical velocity to be continuous across the the interface between the two layers at  $z = z_d$ :

$$\hat{w}(\tilde{z}_d) = C_1 + C_2 \quad (23)$$

$$\partial_{\tilde{z}} \hat{w}(\tilde{z}_d) = i\Lambda_z(C_1 - C_2), \quad (24)$$

since  $\hat{p}(\tilde{z}_d) = -i(U/k)(1 - F^2)\partial_{\tilde{z}}\hat{w}(\tilde{z}_d)$ . Combining (23) and (24) then determines  $C_1$  and  $C_2$ , and the reflection coefficient:

$$r = \left| \frac{\Lambda_z \hat{w}(\tilde{z}_d) + i\partial_{\tilde{z}} \hat{w}(\tilde{z}_d)}{\Lambda_z \hat{w}(\tilde{z}_d) - i\partial_{\tilde{z}} \hat{w}(\tilde{z}_d)} \right|. \quad (25)$$

The solution for  $\hat{w}$  in the absorbing layer is obtained by: 1) specifying the the horizontal scale of the wave in terms of the dimensionless parameters  $K$ ,  $F$  and  $\alpha$ , 2) specifying the depth of the absorbing layer  $\tilde{z}_t - \tilde{z}_d$  and the maximum damping coefficient  $\beta_{max}$  at the top of the layer, and 3) solving (19) for  $\hat{w}$  by inverting a tridiagonal matrix subject to the boundary conditions  $\hat{w}(\tilde{z}_d) = 1$  and  $\hat{w}(\tilde{z}_t) = 0$ . As a check on this analysis procedure, we confirm that by setting  $R_w = 0$  and inserting a damping term  $-K_u \hat{u}$  on the rhs of the horizontal momentum equation (14), we recover the same reflection coefficients as presented by Klemp and Lilly (1978).

To illustrate the reflection characteristics of the proposed absorbing layer, we consider first its behavior for the horizontal scale parameters  $K = F = 0.1$ , which corresponds to  $f/N = KF = 0.01$ . Here,  $K$  is a measure of the nonhydrostatic character of the wave ( $K \rightarrow 0$  in the hydrostatic limit), while  $F$  reflects the influence of inertial effects on the wave. Steady vertically propagating waves are permitted in the parameter range  $K < 1$  and  $F < 1$ . Thus, these small values of  $K$  and  $F$  characterize waves that are nearly hydrostatic with small inertial influences. For reference values of the parameters  $U = 10 \text{ ms}^{-1}$ ,  $N = 10^{-2} \text{ s}^{-1}$ , and  $f = 10^{-4} \text{ s}^{-1}$ , the specification of  $K = F = 0.1$  corresponds to a horizontal wavelength  $\lambda_H = 2\pi/k = 62.8 \text{ km}$ , which would be the maximum energy containing scale for steady linear flow over a bell-shaped mountain having half-width  $a = 10 \text{ km}$ . For the final dimensionless coefficient, we set  $\alpha = 0.1$ . Note that  $\alpha$  is not inherently dependent on horizontal scale since the time step  $\Delta\tau$  typically increases in proportion to the horizontal scale while the horizontal wavenumber  $k$  decreases accordingly.  $\alpha$  can also be expressed as  $\alpha = 2\pi c_r \Delta x / \lambda_H$ , where  $c_r = c\Delta\tau/\Delta x$  is the Courant number for the small time steps, and thus,  $\alpha$  depends principally on the ratio of the horizontal wavelength to the grid scale. For a typical value of  $c_r = 0.5$ ,  $\alpha = 0.1$  corresponds to a horizontal wavelength of about  $30\Delta x$ . This is approximately equivalent to the resolution of the maximum energy wavelength with  $\Delta x = 2 \text{ km}$  for the bell mountain having  $a = 10 \text{ km}$ .

The reflection coefficient  $r$  is plotted in Fig. 1a as a function of  $\beta_{max}$  for various depths of the absorbing layer for  $K = F = \alpha = 0.1$  for the proposed implementation in which the implicit Rayleigh damping on  $w$  is applied in the absorbing layer through an adjustment step (9) in the integration procedure. For this parameter regime, the damping layer provides good absorption of gravity-wave energy for layers at least one vertical wavelength in depth over a broad range of damping coefficients  $\beta_{max}$ . Since  $k$  is contained in  $\beta_{max}$ , the insensitivity of  $r$  to  $\beta_{max}$  is beneficial because it also means that good wave absorption can be achieved

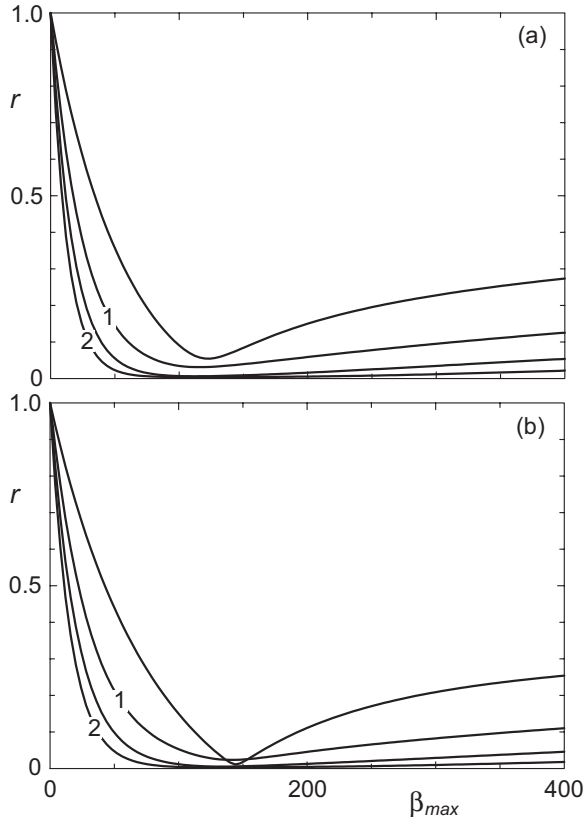


Figure 1. Linear reflection coefficient  $r$  as a function of  $\beta_{max} = R_w(z_t)/kU$  for a single wavenumber  $k$  for  $kU/N = f/kU = 0.1$  with an implicit Rayleigh damping term applied (a) as an adjustment (9) at the end of the time step with  $\alpha = 0.1$ , and (b) directly in the  $w$  equation (7). Reflection characteristics are displayed for  $D/\lambda_z = 0.5, 1.0, 1.5$ , and  $2.0$ , where  $\lambda_z = 2\pi U/N$  represents the vertical wave length for a steady hydrostatic nonrotating mountain wave, and  $D = z_t - z_d$ .

for a given dimensional damping coefficient  $R_w$  over a wide range of horizontal scales.

Figure 1b depicts the reflection characteristics for  $\alpha = 0$ , which corresponds to the case in which an implicit Rayleigh damping term is added directly to the vertical momentum equation (7). For this implementation the damping layer exhibits similarly good absorption characteristics to those in Fig 1a for our proposed scheme, implying that for  $K = 0.1$  the nonhydrostatic influences are still sufficient to provide effective damping.

Moving to larger horizontal scales, Fig. 2 displays the corresponding reflection coefficients for  $K = 0.02$  and  $F = 0.5$ , a five times greater horizontal wavelength than shown in Fig. 1. Here, the damping applied through an adjustment step with  $\alpha = 0.1$  (Fig. 2a) can provide an effective absorption layer, similar to the behavior at shorter scales as depicted in Fig.1a. However,

if the Rayleigh damping term is applied directly within the vertical momentum equation (Fig. 2b for  $\alpha = 0$ ), the reflection of gravity-wave energy is increased significantly. The differing impact of implementing Rayleigh damping directly in (7) or as an adjustment step (9) is apparent from equation (19). Applying the damping directly in the  $\hat{w}$  equation produces the damping term in the coefficient multiplying  $\hat{w}$  in (19):  $1 - K^2(1 - i\beta_w)$ . As the flow becomes sufficiently hydrostatic ( $K \rightarrow 0$ ) the influence of this damping term disappears. In contrast, when the Rayleigh damping is applied as an adjustment step, the term multiplied by  $\alpha$  in (19) is also present and remains effective even in the limit of hydrostatic flow. For inertia gravity waves the absorbing layer may have increased effectiveness at larger horizontal scales since the vertical wavelength decreases with increasing  $F$  (i.e.  $\lambda_z \sim \sqrt{1 - F^2}$ ). Although the behavior of the absorbing layer is illustrated in Fig. 2 for  $\alpha = 0.1$ , similar behavior can be inferred for other values of  $\alpha$ . Since the damping term in (19) is proportional to  $\alpha^2\beta_w$  larger values of  $\alpha$  (higher wavenumbers, closer to the grid scale) yield the same reflection characteristics for a smaller value of the damping coefficient  $\beta_w$ . As  $K$  is decreased further below 0.02, the reflection profiles

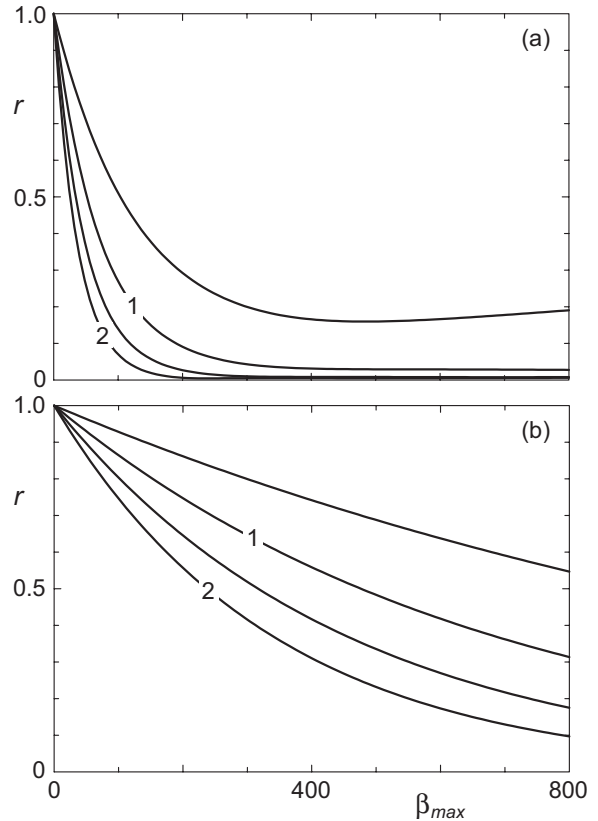


Figure 2. As in Fig. 1 except for a five times larger horizontal wavelength corresponding to  $kU/N = 0.02$  and  $f/kU = 0.5$ .

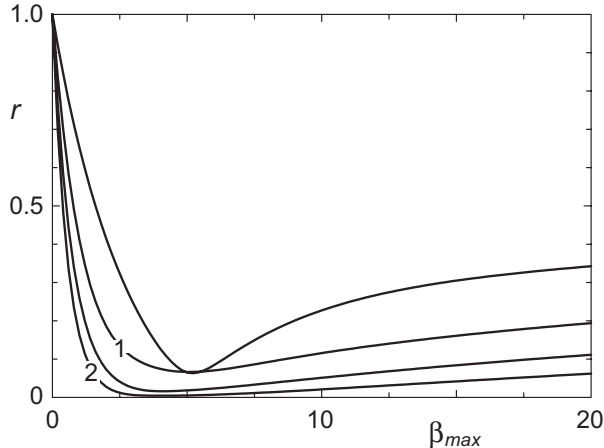


Figure 3. As in Fig. 1 except for a five times smaller horizontal wavelength corresponding to  $kU/N = 0.5$  and  $f/kU = 0.02$ .

shown in Fig. 2b move closer to unity, while the profiles in Fig. 2a remain little changed.

At smaller horizontal scales where nonhydrostatic effects are significant, the Rayleigh damping effects inherent in the  $w$  equation dominate, and thus applying the Rayleigh damping either directly in the vertical momentum equation (7) or as an adjustment step (9) yields virtually identical results. Fig. 3 displays the reflection coefficient  $r$  as a function of  $\beta_{max}$  for a horizontal wavenumber  $K = 0.5$  that is five times larger than the wavenumber considered in Fig. 1. Here, the reflection characteristics as a function of the depth of the absorbing layer are similar to those at larger scales except that the values of  $\beta_{max}$  are much reduced.

#### 4. Linear mountain wave simulations

To document the practical application of our proposed absorbing layer, we consider first the case of uniform flow over a small amplitude ( $h_m = 10$  m) bell-shaped mountain. The linear analytic solutions for the resulting steady mountain waves are well documented for a wide range of horizontal scales (see for example Smith 1979) and are frequently used to test the viability of various aspects of model numerics. For these simulations, we utilize a split-explicit time integration of the full 2-D nonhydrostatic equations cast in terms of a terrain-following hydrostatic pressure (mass) coordinate [see Klemp et al. (2007) and analysis in the Appendix], using an Arakawa C-grid staggering for variables on the computational grid. The large time steps are advanced using leapfrog time differencing and the advection terms are represented by second order centered differences. (Choice of the large time step integration scheme, such as leapfrog or Runge-

Kutta, has no effect on the implementation of the absorbing layer). The undisturbed atmospheric flow is characterized by a constant cross mountain velocity  $U = 10 \text{ ms}^{-1}$  and constant Brunt-Väisälä frequency  $N = 0.01 \text{ s}^{-1}$ , which produce a vertical wavelength  $\lambda_z = 2\pi U/N = 6.28 \text{ km}$  for steady hydrostatic mountain waves in the absence of rotation. To represent these waves on the model grid, we employ a nearly constant vertical grid spacing  $\Delta z \simeq 250 \text{ m}$ .

We first consider a mountain-half width  $a = 10$  km, for which the steady linear mountain waves are nearly hydrostatic and rotational influences are small. We set the horizontal grid length at  $\Delta x = 2 \text{ km}$ , and the large and small time steps are 24 s and 4 s, respectively. The damping layer begins at  $z_d = 10 \text{ km}$  and extends to the top of the domain at  $z_t = 20 \text{ km}$ , with the Rayleigh damping coefficient specified according to (21) with a maximum value  $R_w(z_t) = 0.15 \text{ s}^{-1}$ . Recognizing that the maximum energy containing scale occurs at  $k = a^{-1}$ , we can estimate the dimensionless parameters in the previous section for this scale:  $K = F = 0.1$ ,  $\alpha = 0.12$ ,  $D/\lambda_z = 1.6$ , and  $\beta_{max} = 150$ . The parameters  $K$ ,  $F$ , and  $\alpha$  correspond closely to the conditions represented in Fig. 1a and the values of  $D$  and  $\beta_{max}$  indicate there should be little reflection of vertically propagating wave energy. Fig. 4a displays the linear steady-state solution for the vertical velocity field while Fig. 4b shows the corresponding numerical solution. Here, the linear steady-state solution is obtained through Fourier reconstruction from the analytic solutions for the individual horizontal wave numbers. For convenience, we shall henceforth refer to these linear solutions as the “analytic” solutions. The numerical integration was carried out to 30 h (dimensionless time  $Ut/a=108$ ) to ensure that any wave reflection from the upper boundary would have sufficient time to affect the entire domain. The corresponding vertical momentum flux profile at this time is shown in Fig. 5, and should be compared against the constant theoretical value  $M/M_H = 0.94$  (see Klemp and Lilly, 1980). The close agreement between the numerical and analytical solutions for  $w$  and  $M$  in the inviscid region below 10 km confirms the effectiveness of the Rayleigh damping layer for  $w$  at this horizontal scale.

We also simulated this case using a shallower absorbing layer by lowering the top of the domain to  $z_t = 15 \text{ km}$ , while keeping  $z_d$  at 10 km ( $D/\lambda_z = 0.8$ ). The resulting vertical velocity field at  $Ut/a = 108$ , shown in Fig. 4c, retains reasonably good quantitative agreement with the analytic solution in Fig. 3a, although a slight distortion of the contours is apparent due to partial wave reflection. The momentum flux profile in Fig. 5 also remains close to the theoretical value.

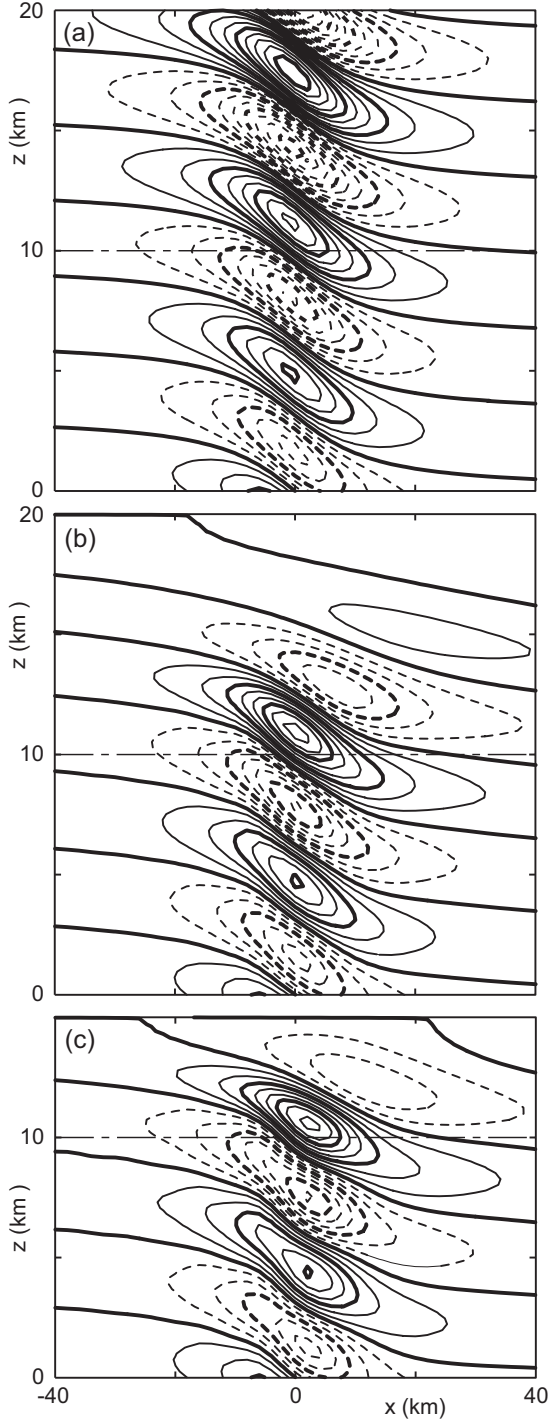


Figure 4. Vertical-velocity contours for flow with constant mean wind and stability passing over a 10 m bell-shaped mountain of half-width  $a = 10$  km ( $U/aN = 0.1$  and  $af/U = 0.1$ ). (a) Linear analytic solution for steady inviscid vertically propagating mountain wave. (b) Numerical simulation at  $Ut/a = 108$  with absorbing layer between  $z = 10$  km (indicated by the thin dot-dashed line) and  $z_t = 20$  km ( $D/\lambda_z = 1.6$ ). (c) As in (b) except with  $z_t = 15$  km ( $D/\lambda_z = 0.8$ ). The contour interval is  $0.002 \text{ ms}^{-1}$ , with every third contour represented by a heavier line.

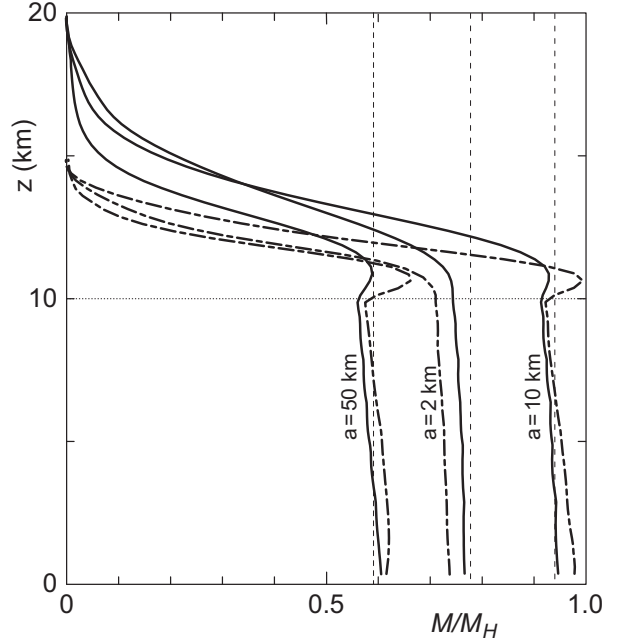


Figure 5. Vertical momentum flux profiles at  $Ut/a = 108$  for the numerical simulations shown in Figs. 4, 6, and 7, with the damping layer extending from 10 km up to top of the model domain at  $z_t = 20$  km ( $D/\lambda_z = 1.6$ , plotted with solid lines) and for a model top at  $z_t = 15$  km ( $D/\lambda_z = 0.8$ , plotted with dot-dashed lines). Profiles are displayed for  $K = U/aN = 0.5, 0.1$  and  $0.02$ , corresponding to a mountain halfwidth  $a = 2$  km, 10 km, and 50 km, respectively. Profiles are normalized with respect to the steady linear momentum flux  $M_H$  for hydrostatic nonrotating flow, and the corresponding theoretical constant-flux profiles (Klemp and Lilly, 1980) are indicated by the short-dashed lines.

To test this damping layer at larger scales, we increased the mountain half-width by a factor of 5 to  $a = 50$  km. For this simulation, the horizontal grid length  $\Delta x = 10$  km and the large and small time steps  $\Delta t = 120$  s and  $\Delta \tau = 20$  s are proportionately larger. For the maximum energy containing scale  $k = a^{-1}$ , the parameters  $K = 0.02$ ,  $F = 0.5$ , and  $\alpha = 0.12$  correspond closely to those used in calculating the damping-layer reflection characteristics displayed in Fig. 2a. The maximum damping coefficient at the top of the absorbing layer is set at  $R_w(z_t) = 0.05 \text{ s}^{-1}$ , which corresponds to  $\beta_{max} = 250$ .

The vertical velocity field at  $Ut/a = 108$  for the simulation with  $z_t = 20$  km ( $D/\lambda_z = 1.6$ ) is displayed in Fig. 6b, and again exhibits close agreement below 10 km with the analytic solution shown in Fig. 6a. The vertical momentum flux profile below 10 km also agrees well with the constant analytic value of  $M/M_H = 0.59$  (Klemp and Lilly 1980). Lowering the top of the model domain to 15 km ( $D/\lambda_z = 0.8$ ), again reveals slight distortion in the vertical velocity field (Fig. 6c),

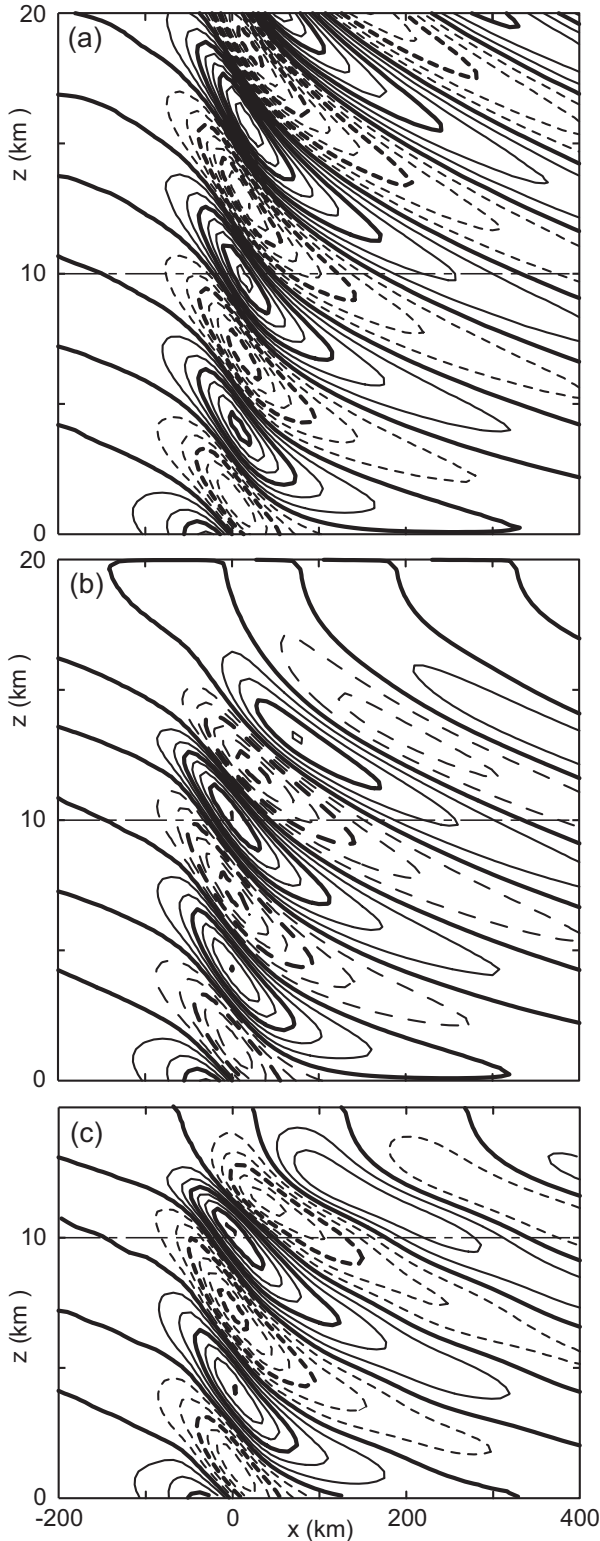


Figure 6. As in Fig. 4 except for a mountain half-width  $a = 50$  km ( $N/aU = 0.02$  and  $af/U = 0.5$ , and the contour interval is  $0.0003 \text{ ms}^{-1}$ ).

although the overall agreement with the analytic solution is reasonably maintained. Similarly, the momentum flux profile in Fig. 5 remains near the analytic value, although with a larger deviation just above the top of the inviscid region.

To evaluate the behavior at smaller nonhydrostatic scales, we reduced the mountain half-width to  $a = 2$  km and scaled down the grid characteristics accordingly ( $\Delta x = 400$  m,  $\Delta t = 4.8$  s and  $\Delta \tau = 0.8$ ). For the representative wavenumber  $k = a^{-1}$ , the parameters  $K = 0.5$ ,  $F = 0.02$ , and  $\alpha = 0.12$  are similar to those represented in Fig. 3. We specified the maximum Rayleigh damping coefficient  $R_w(z_t) = 0.04 \text{ s}^{-1}$ , corresponding to  $\beta_{max} = 7.5$ , which is consistent with good absorption characteristics in Fig. 3. Here again, the simulation with a 10 km deep absorbing layer ( $D/\lambda_z = 1.6$ ), shown in Fig. 7b, exhibits good agreement with the linear analytic solution in Fig. 7a in the inviscid region below 10 km. At these scales, the characteristic nonhydrostatic behavior is clearly evident in the downstream displacement of the waves with height. Reducing the depth of the absorbing layer by half to  $D/\lambda_z = 0.8$  maintains the upward radiating character of the waves, although slight distortions in the wave structure are evident (Fig. 7c). Similarly, the vertical momentum flux profile shown in Fig. 5 is very close to the linear analytic value of  $M/M_H = 0.78$  in the inviscid region below 10 km for the 10 km deep absorbing layer, and degrades only slightly when the absorbing layer thickness is reduced to 5 km.

## 5. Idealized squall-line simulations

To test the behavior of this implicit gravity-wave absorbing layer in a more complex environment, we consider the simulation of convective squall lines, which are known to produce a broad spectrum of gravity waves radiating upward and laterally from the convective region. For this purpose, we simulate an idealized two-dimensional squall line using the WRF/ARW version 2.2 (Skamarock et al. 2005, Klemp et al. 2007, Skamarock and Klemp, 2007). The WRF/ARW solves the nonhydrostatic equations using a terrain-following hydrostatic-pressure (mass) vertical coordinate, and thus the implicit Rayleigh damping layer is implemented as described in the Appendix. The atmosphere is initialized with the horizontally homogeneous thermodynamic sounding created by Weisman and Klemp (1982) together with a wind profile having  $U = -12 \text{ ms}^{-1}$  at the surface, increasing linearly to zero at  $z = 2.5$  km, and remaining constant at zero above this height. With this environmental shear, a long-lived squall line develops with a pulsing regeneration of the active convection that gradually decays over time, consistent with the results of Rotunno et

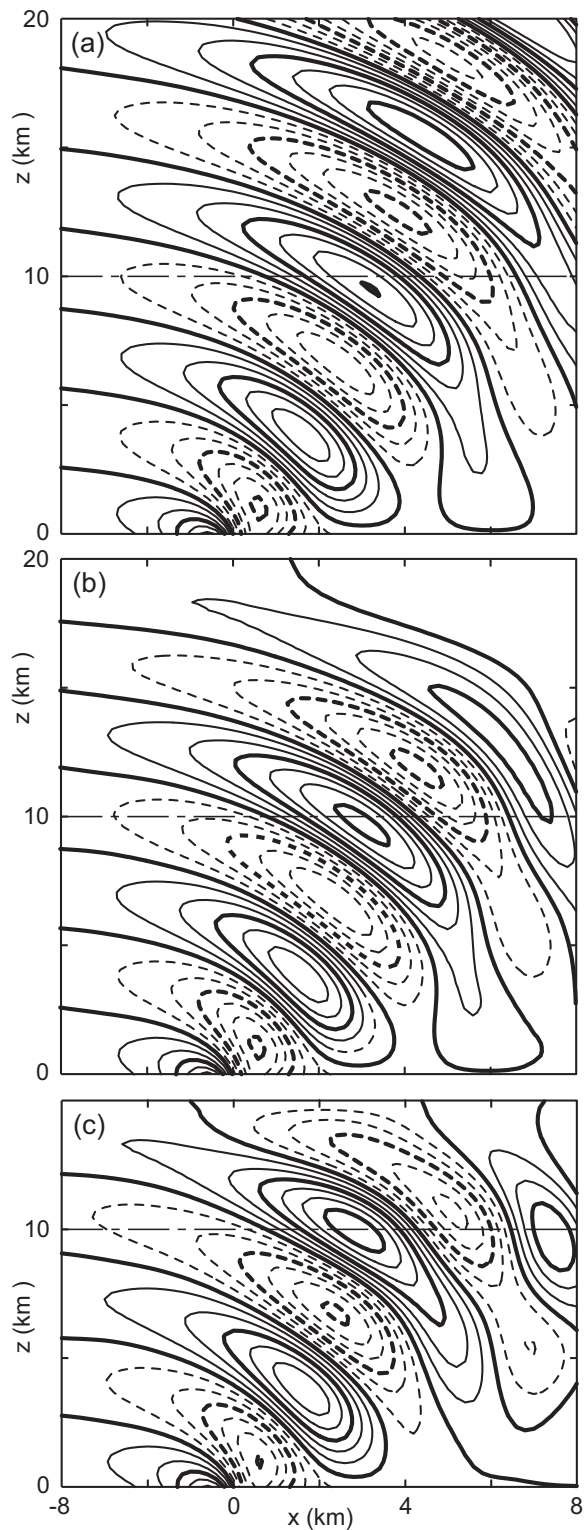


Figure 7. As in Fig. 4 except for a mountain half-width  $a = 2$  km ( $N/aU = 0.5$  and  $af/U = 0.02$ , and the contour interval is  $0.006 \text{ ms}^{-1}$ ).

al (1988) and Weisman et al (1988). The model domain extends 500 km in the horizontal and 30 km in the vertical with a nominal 250 m grid size in both directions. In the time-split numerical integration, the large time step is  $\Delta t = 2$  s, and the small time step is  $\Delta \tau = 0.5$  s. The absorbing layer is located between 20 and 30 km, with the Rayleigh damping coefficient increasing with height according to (21).

Vertical cross-sections of the simulated squall line both with the absorbing layer ( $R_w = 0.2 \text{ s}^{-1}$ ) and with no absorbing layer ( $R_w = 0$ ) are displayed in Fig. 8 at 1, 3, and 5 h. At 1 h, the gravity waves generated by the squall line are just reaching the top of the domain, and thus the two simulations are quite similar. By 3 h, significant reflection from the upper boundary is evident in the simulation with no absorbing layer, and by 5 h the entire stratosphere is altered by these reflected modes. In contrast, with the absorbing layer, the upward propagating gravity waves are gradually damped out above 20 km with little evidence of reflection. Here, the most energetic modes have a horizontal wavelength of about 40 km and a phase speed of about  $20 \text{ ms}^{-1}$ . Given the mean stratospheric stability of about  $N = 0.02 \text{ s}^{-1}$ , the absorbing-layer depth is about 1.5 times the vertical wavelength ( $2\pi U/N$ ) of these waves.

We also conducted simulations of this squall line with smaller ( $R_w = 0.1 \text{ s}^{-1}$ ) and larger ( $R_w = 0.4 \text{ s}^{-1}$ ) values of the maximum Rayleigh damping coefficient. From these simulations, we concluded that  $R_w = 0.2 \text{ s}^{-1}$  provided the best overall absorption of the gravity waves; with the smaller value the waves retained finite amplitude at the top of the domain, and with the larger value, most of the wave amplitude was removed in the lower portion of the absorbing layer. For a more quantitative assessment, we computed the vertical energy flux  $\langle pw \rangle$  for these simulations, which is displayed in Fig. 9 for the upper portion of the computational domain. Here, the energy flux profiles are more informative than those for vertical momentum flux since they are always positive for upward propagating wave energy, while the momentum flux is positive for rightward-propagating gravity waves but negative for leftward moving ones. The energy flux is quite variable in response to the pulsating character of the convective updrafts and thus small differences the squall-line evolution can result in large differences in the energy-flux profiles in the stratosphere. However, the behavior within the absorbing layer is consistent with our expectations: with no damping the energy flux profile oscillates significantly in the upper 10 km of the domain and even becomes negative at times (i.e. at 5 h as shown in Fig. 9c) as a consequence of the reflected modes. With the absorbing layer turned on ( $R_w = 0.1 - 0.4 \text{ s}^{-1}$ ) the energy flux

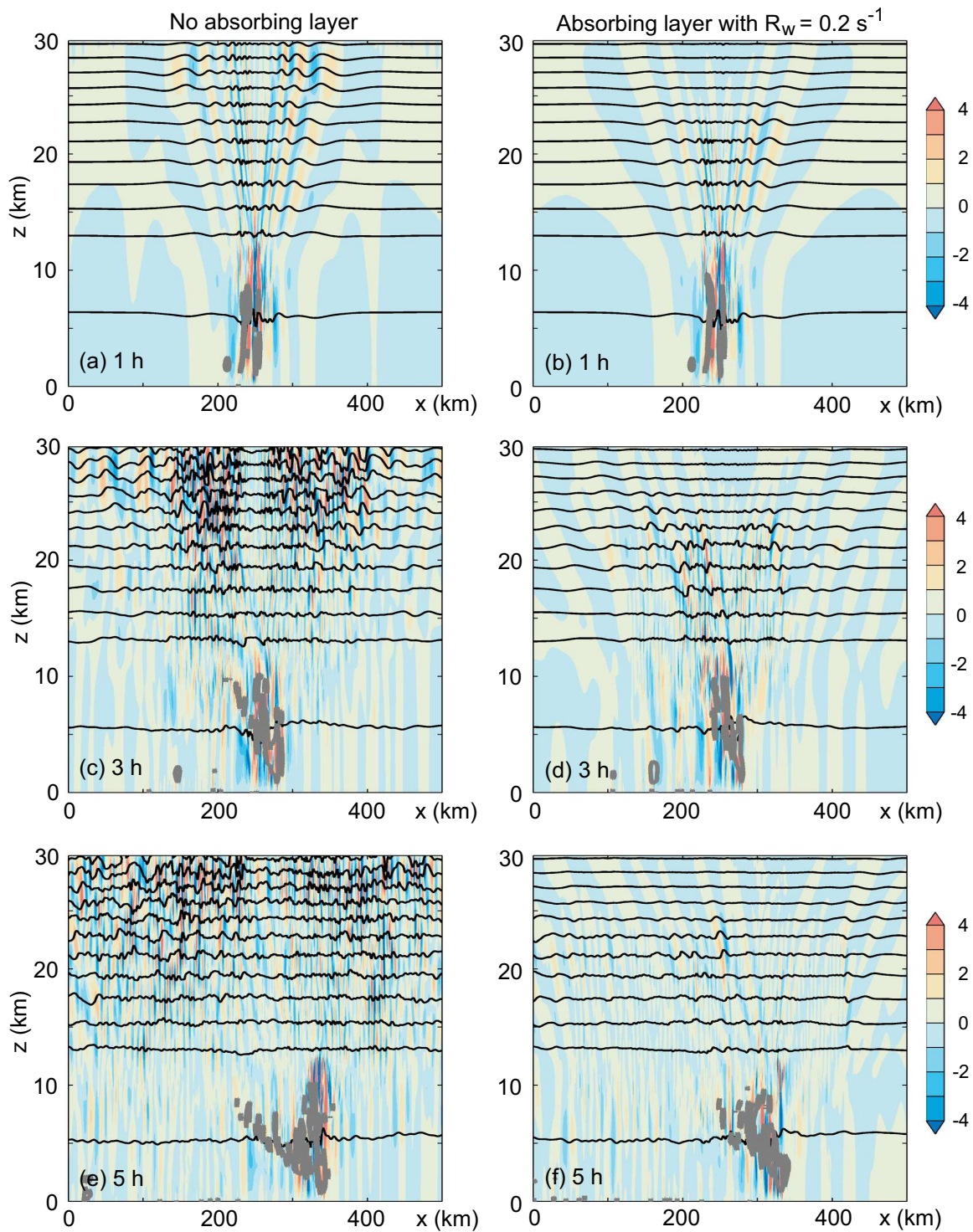


Figure 8. Vertical cross-sections for 2-D squall line simulations at 1, 3, and 5 h with no upper absorbing layer (panels a, c, and e) and with a 10 km deep absorbing layer (20-30 km) with  $R_w = 0.2 \text{ s}^{-1}$  (panels b, d, and f). The line contours represent the potential temperature (40 K contour interval), the color contouring depicts the vertical velocity (scale in  $\text{m s}^{-1}$ ), and the gray shading indicates the region in which the cloud-water concentration exceeds  $0.2 \text{ g kg}^{-1}$ .

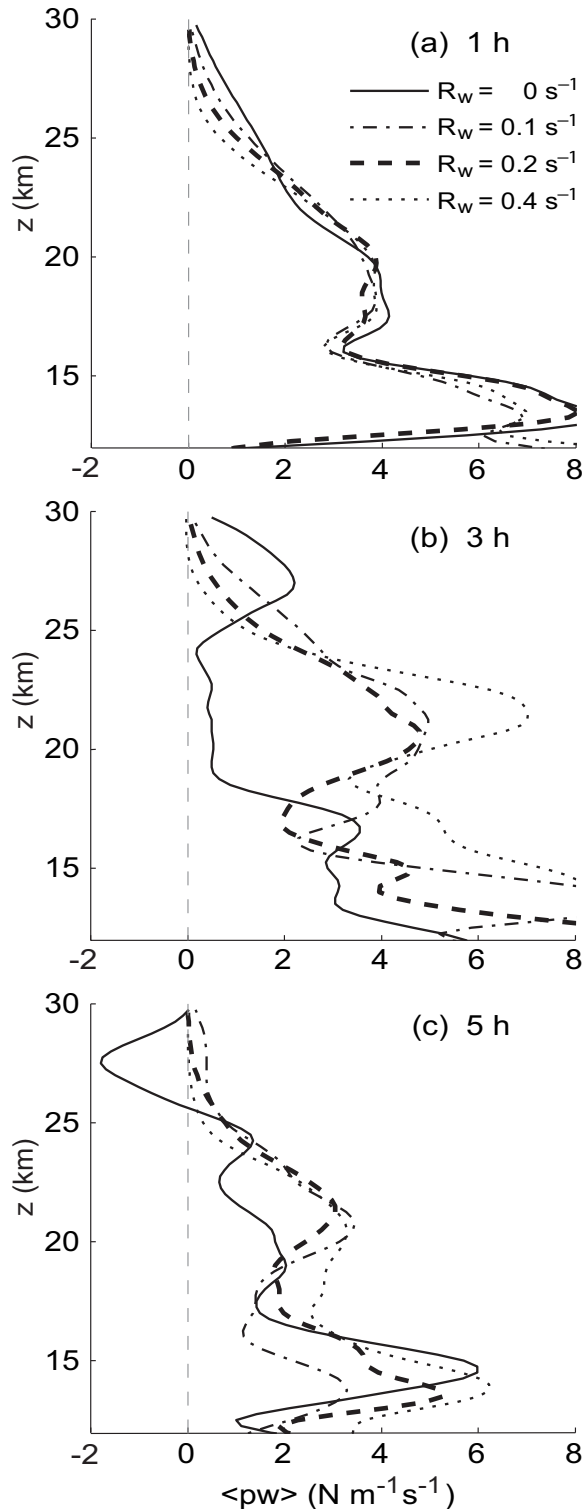


Figure 9. Vertical energy flux  $\langle pw \rangle$  profiles between 12 and 30 km at 1, 3, and 5 h for a simulation with no absorbing layer ( $R_w = 0$ , solid lines), and for simulations having a 10 km deep absorbing layer with  $R_w = 0.1$ , 0.2, and 0.4, depicted by dot-dashed, heavy dashed, and dotted lines, respectively, as labeled in the figure.

decays monotonically with height above about 20 km, although a slight oscillation near the upper boundary is still apparent for  $R_w = 0.1 \text{ s}^{-1}$  at 5 h (Fig. 9c). With increasing  $R_w$  the energy flux decreases more rapidly with height, consistent with the remarks above regarding the observed decline of the wave amplitude. While there is no precise means of determining the “optimal” value of  $R_w$ , setting  $R_w = 0.2 \text{ s}^{-1}$  appears to produce the best overall results for this case.

## 6. NWP simulation over the Colorado Rocky Mountains

The implicit Rayleigh absorbing layer proposed here should be particularly well suited for NWP applications, for which there is no rigorous way to separate the gravity-waves from the evolving larger-scale flow. We demonstrate the NWP application of this absorbing layer in a retrospective forecast for a case of large-amplitude mountain waves over the eastern slope of the Colorado Rocky Mountains on 4-5 December 2007. From about 12/04/07 12 UTC to 12/05/07 12 UTC, strong downslope winds persisted along the eastern slope of the Colorado Rockies; during this period, the maximum winds at the NCAR Mesa site in Boulder, Colorado were in the range 20-30  $\text{ms}^{-1}$ , while at the NCAR Foothills site (260 m lower elevation and several kilometers farther east) the winds were 15-25  $\text{ms}^{-1}$ . For this case, we have rerun the NCAR WRF/ARW real-time forecast for the west-central U.S. (see [http://www.wrf-model.org/plots/realtime\\_main.php](http://www.wrf-model.org/plots/realtime_main.php)) initialized at 00 UTC on 12/04/07. The model is run in a nested configuration, with a 30 km grid outer domain covering the continental U.S. and a 2200x2000 km inner domain over the west-central U.S. with a 10 km grid as shown in Fig. 10. The initial fields were interpolated from the 40 km NCEP NAM analysis, while the boundary conditions for the outer domain were interpolated from the NAM forecast. The 10 km nested domain is integrated with a 60 s large time step and a 15 s small time step. This period of 4-5 December was characterized by strong west-northwestly flow over the Colorado Rockies (about 20  $\text{ms}^{-1}$  at 700 mb), which is conducive to producing strong mountain waves and downslope winds on the eastern slope.

In the numerical forecasts, significant terrain-generated gravity waves developed rapidly throughout the Rocky mountains in response to the strong tropospheric westerly flow. This is evident in the vertical velocity cross section at  $z = 10$  km at 12 h in Fig. 10, particularly over the eastern slope of the Colorado Rockies. The vertical cross section along the line indicated in Fig. 10 is displayed in Fig. 11a and 11b at 12 and 30 h, respectively, for the

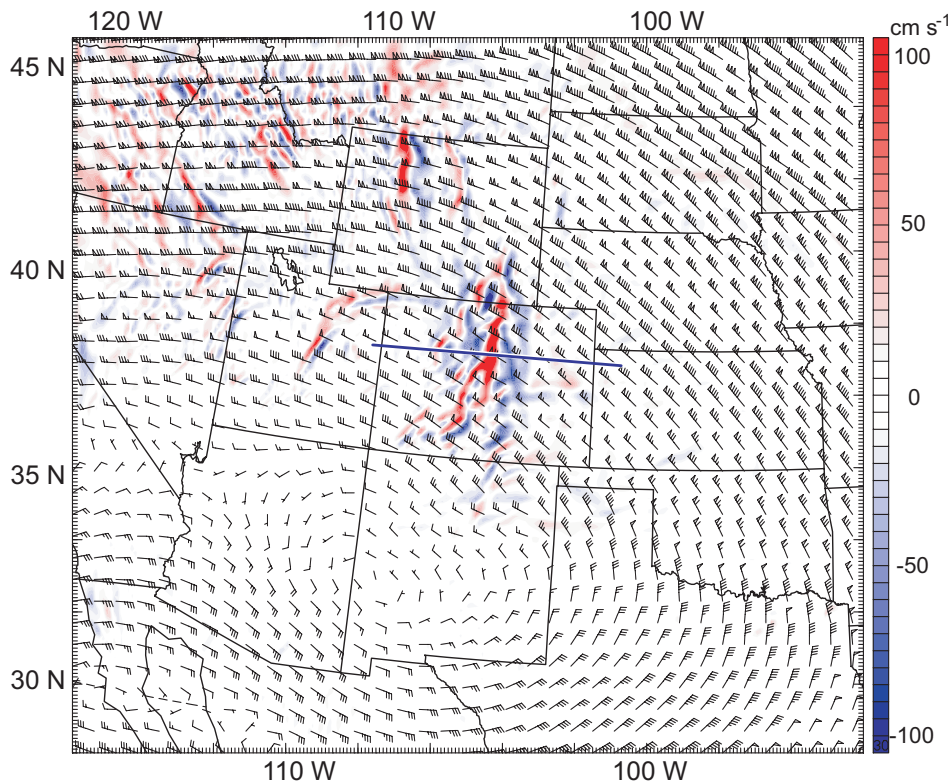


Figure 10. Nested 10 km grid domain for retrospective forecasts initialized at 00 UTC 4 December 2007. The vertical velocity (red/blue shading) and horizontal velocity (wind barbs in knots) are displayed at 12 h into the forecast at  $z = 10$  km, with the top of the model domain set at 50 mb. The heavy blue line indicates the location of the vertical cross sections displayed in Fig. 11.

simulation with the model top at 50 mb, with a 5 km deep absorbing layer beneath the top having a maximum damping coefficient  $R_w = 0.2 \text{ s}^{-1}$ . At 12 h, the large amplitude standing mountain wave above the eastern slope is clearly evident. The maximum updraft and downdraft velocities are about  $\pm 3 \text{ ms}^{-1}$  on this 10 km grid, and the maximum surface wind occurs about half way down the lee slope, with a maximum of about  $40 \text{ ms}^{-1}$  at 12 h, and decreasing to about  $30 \text{ ms}^{-1}$  at 30 h. Winds at the base of the slope were around  $20 \text{ ms}^{-1}$  during this period. For this configuration, we found that while the absorbing layer had significant effect in removing the gravity waves present in the lower stratosphere, the corresponding simulation with no absorbing layer (not shown) had virtually the same wave structure throughout the troposphere. We believe this occurs because in this particular case the large-amplitude waves in the troposphere overturn and dissipate near the tropopause and thus are not significantly affected by the presence or absence of the absorbing layer in the lower stratosphere. Because of this relative insensitivity, we will treat this simulation as a reference in further sensitivity testing.

To achieve a more discriminating assessment of the effects of the absorbing layer for this case, we lowered the model top from 50 mb to 100 mb (from 20 km to about 16 km). Including the absorbing layer in the upper 5 km of the model domain, we obtain a mountain-wave structure over the lee slope of the Colorado Rockies at 12 and 30 h as shown in Fig. 11c and 11d, respectively. In comparison to the deeper-domain simulation (Fig. 11a-b), the wave structure throughout the troposphere is quite similar, although the wave amplitude just above the tropopause ( $\sim 12$ - $13$  km) is clearly reduced as the absorbing layer becomes stronger with increasing height. In contrast, the simulation with the model top at 100 mb and no absorbing layer (Fig. 11e-f) exhibits significant distortion of the waves in the troposphere due to wave reflection from the upper boundary. At 12 h, reflection of the primary wave is apparent (Fig. 11e) in the updraft over the lee slope that spans the troposphere. With vertically radiating wave energy, this updraft is continuous and tilts upstream (westward) with increasing height, as in the simulations with an absorbing layer (Fig. 11a and 11c). However, in Fig. 11e the updrafts and

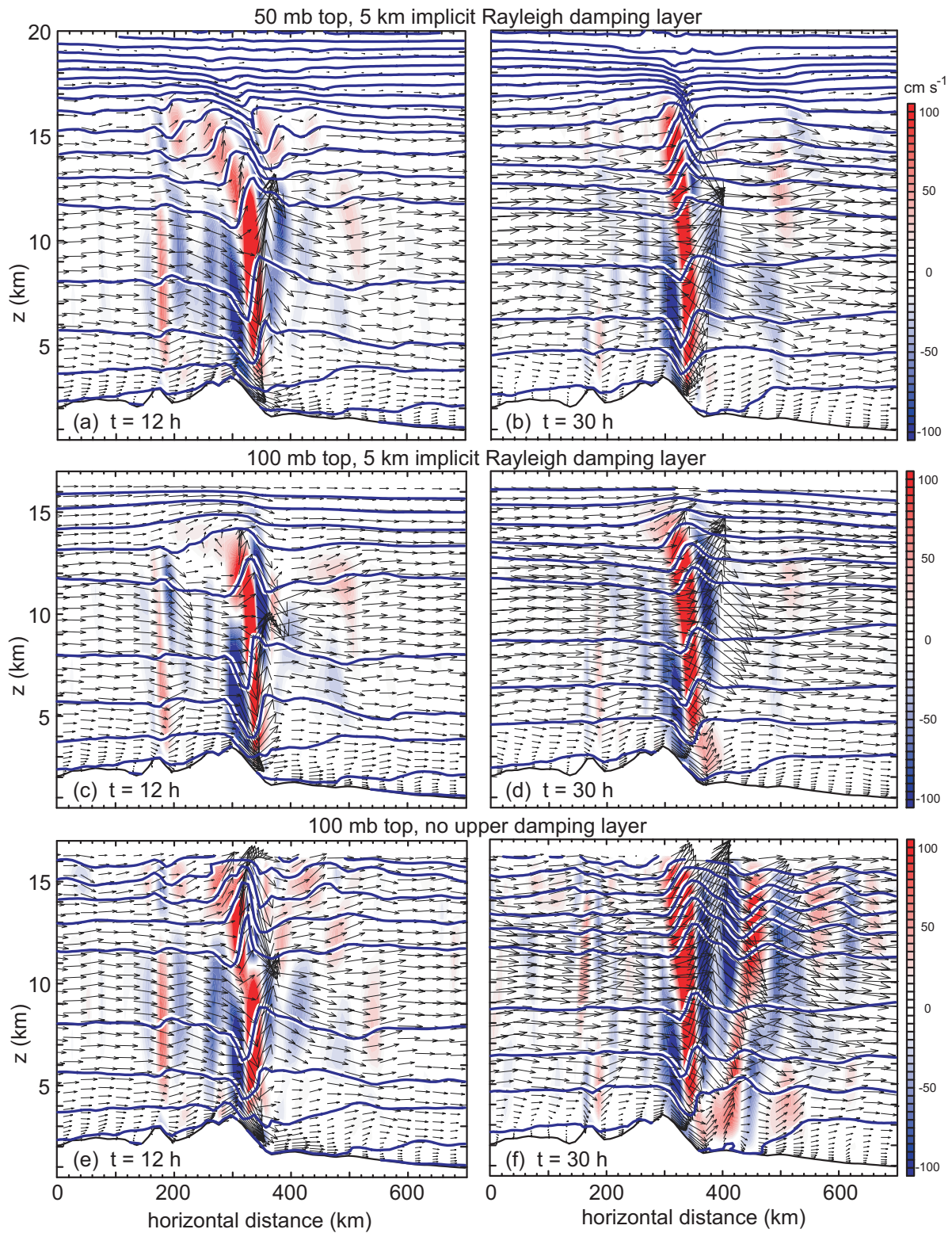


Figure 11. Vertical cross sections of flow over the eastern slope of the Colorado Rockies as indicated in Fig.10 for retrospective forecasts initialized at 00 UTC 4 December 2007. The vertical velocity (red/blue shading), potential temperature (contoured in heavy blue lines, with 10 K contour intervals, beginning at 300 K near the surface), and wind vectors in the vertical plane are shown at 12 and 30 h into the forecast for the model configuration with: (a)-(b) the domain top at 50 mb and the implicit Rayleigh damping layer in the upper 5 km, (c)-(d) the domain top at 100 mb and the implicit Rayleigh damping layer in the upper 5 km, and (e)-(f) the domain top at 100 mb with no upper absorbing layer.

upper boundary. By 30 h, the reflected wave energy has also moved downstream of the primary wave and further distorted the wave structure throughout the vertical extent of the domain (Fig. 11f). Here, we have not attempted to optimize the strength and depth of the absorbing layer for this simulation, but rather have configured the layer as might be done in NWP models where there may be constraints on increasing the height of the model top significantly to accommodate an absorbing layer.

## 7. Summary and Discussion

Preventing the artificial reflection of gravity-wave energy from the upper boundary of a mesoscale simulation domain for NWP applications remains a significant challenge. Here, we have proposed a new formulation for an upper absorbing layer that appears to function effectively across the range of horizontal scales for which the vertical propagation of internal gravity-wave energy may be significant. This approach is designed for split-explicit time-integration schemes and is implemented as an implicit Rayleigh damping term for the vertical velocity, applied as a final adjustment step at the end of each small (acoustic) time step. This procedure does not relax the flow back to a specified reference state, as occurs in traditional absorbing layers in which Rayleigh damping terms are applied to all of the dynamical prognostic variables. The approach also is not restricted by the linear stability constraints that limit the effectiveness of absorbing layers that utilize second (or higher) order diffusion to remove gravity-wave energy. While the proposed absorbing layer does not reduce the requirements for the depth of the layer (typically one vertical wave length or greater), it does appear better suited for use in the more complex environments of NWP applications.

In the example applications we have presented, the values of  $R_w$  used for the respective simulations were chosen with some experimentation to provide the best overall behavior of the absorbing layer. To provide more general guidance in selecting an appropriate value for any particular application, we return to the linear analysis for steady mountain waves presented in section 3 (which also applies to propagating waves) and replot the reflection coefficient  $r$  as a function of the wavelength of the gravity wave  $\lambda_H = 2\pi/k$  for specified values of  $R_w$ . This is displayed in Fig. 12 for an absorbing layer that is one vertical wavelength in depth. While the length scale is written in dimensionless form, for discussion purposes one can translate readily into dimensional terms by interpreting the horizontal axis labels as the horizontal wavelength in km (i.e.  $U/N \simeq 1000$ ). Similarly, the dimensional maximum damping coefficient  $R_w$  can be estimated

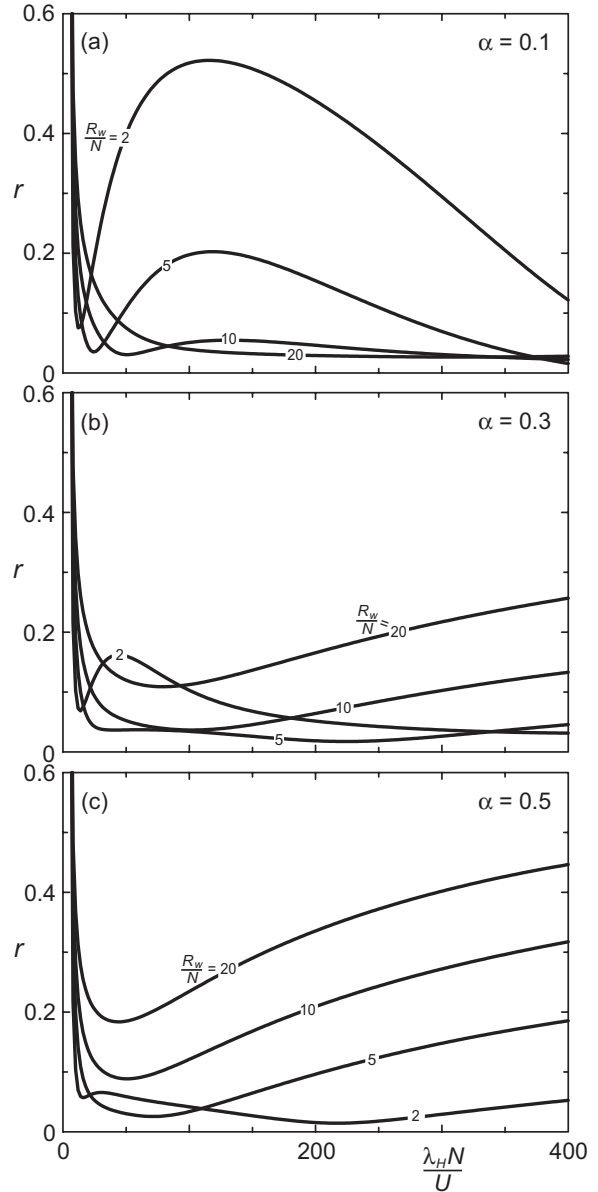


Figure 12. Linear reflection coefficient  $r$  for a single wave number displayed as a function of horizontal wavelength  $\lambda_H N/U = 2\pi/K$ , for a Rayleigh damping layer one vertical wave length in depth with having coefficients of magnitude  $R_w/N = 2, 5, 10,$  and  $20$  for (a)  $\alpha = 0.1$ , (b)  $\alpha = 0.3$ , and (c)  $\alpha = 0.5$ .

from the dimensionless form  $R_w/N$  using  $N = 0.02 \text{ s}^{-1}$  as a typical estimate for the stability in the stratosphere. Since the reflection characteristics also depend on  $\alpha = kc\Delta\tau = k\Delta x c_r$ , we have included plots for  $\alpha = 0.1, 0.3,$  and  $0.5$ . The Courant number might typically be  $c_r \simeq 0.5$ , and thus  $\alpha$  is in effect a measure of how well a wave is resolved on the horizontal grid. For example, in the simulations discussed in sections

4 and 5, the dominant wave modes are generally well resolved (about  $30\Delta x$ ) such that  $k\Delta x \simeq 0.2$ , and  $\alpha \simeq 0.1$ . Consequently, for these well-resolved waves, Fig. 12a suggests that for horizontal wave lengths greater than about 30 km, a value of  $R_w/N \simeq 10$  may be a reasonable estimate for the Rayleigh damping coefficient, and that below 30 km, correspondingly smaller values of  $R_w$  should be considered. For the mountain wave simulations having mountain half-widths  $a = 2, 10, \text{ and } 50$  km (and for which the dominant horizontal wavelengths are  $2\pi a$ ), the Rayleigh damping coefficients that appeared to provide the best overall results were  $R_w/N \simeq 4, 15, \text{ and } 5$ , respectively. These damping coefficients are reasonably consistent with guidance suggested above, although the value of  $R_w/N = 5$  chosen for largest mountain width is somewhat smaller than the “best” values suggested by the curves in Fig. 12a. For the squall-line simulations,  $R_w/N \simeq 10$  appeared to give the best results, which is in agreement with the optimal value in Fig. 10a for a 40 km horizontal wavelength.

For waves that are not well resolved, the effective value of  $\alpha$  will be larger, suggesting that smaller values of  $R_w$  should be considered, as indicated by the curves displayed in Figs. 12b and 12c. For  $\alpha = 0.3$ ,  $R_w/N \simeq 5$  appears to be the best choice over the range of hydrostatic horizontal scales, while for  $\alpha = 0.5$ ,  $R_w/N \simeq 2$ , becomes a better overall value. We confirmed this behavior by simulating mountain waves above a sinusoidal (single wavenumber) mountain having a wavelength of 120 km. For simulations with  $\Delta x = 4$  km ( $\alpha \simeq 0.1$ ) and with  $\Delta x = 20$  km ( $\alpha \simeq 0.5$ ), we verified (results not shown) that with an absorbing layer one vertical wavelength in thickness, the best radiation characteristics were achieved for  $R_w/N \simeq 10$  and  $R_w/N \simeq 2$ , respectively. In fact, the smaller value of  $R_w/N$  mentioned above for the  $a = 50$  km mountain-wave simulation may also be consistent with a larger effective value of  $\alpha$ . Since the inertia-gravity waves at these scales are dispersive, smaller horizontal wavelengths begin to dominate in the absorbing layer at high levels above the mountain, corresponding to larger values of  $\alpha$  that would suggest a smaller value of  $R_w$  (i.e. as in Fig.12b). For the NWP simulation in section 6, the prominent mountain waves ( $\lambda_H \simeq 120$  km) are moderately resolved ( $\alpha \simeq 0.25$ ), and the value of  $R_w/N \simeq 10$  used is consistent with values suggested by Figs. 12a-b.

The reflection coefficients discussed in section 3 and summarized in Fig.12 have been computed assuming that the vertical structure of the wave is well resolved on the computational grid. If the vertical wave structure is not well resolved, the proposed absorbing layer will be correspondingly less effective. This is also true for other types of

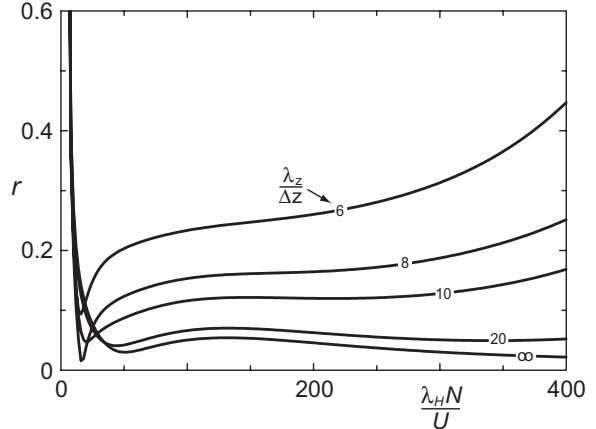


Figure 13. As in Fig. 12a except displaying the linear reflection coefficient  $r$  for  $R_w/N = 10$  for differing vertical grid resolutions, expressed in terms of grid points per vertical wave length,  $\lambda_z/\Delta z$ .

Rayleigh-damping or diffusion absorbing layers (i.e. Klemp and Lilly, 1978). To illustrate the effect of limited vertical resolution, we display in Fig. 13 the reflection coefficient for  $\alpha = 0.1$  and  $R_w/N = 10$  for an absorbing layer that is one vertical wave length in depth as a function of the number of grid points per vertical wavelength [employing second order finite differencing in evaluating (19)]. The curve labeled  $\infty$  thus corresponds to the curve in Fig.12a labeled 10. Clearly, the reflection increases with decreasing resolution, although even at eight points per wavelength the reflection coefficient remain less than 20 percent over most of the range of horizontal scales shown. For NWP applications the vertical grid stretching often results in limited resolution near the top of the model domain. However, even a partial elimination of wave reflection may have substantial benefit, as evidenced in the mountain wave simulation shown in Fig.11, in which both the thickness of and the vertical resolution within the absorbing layer are clearly suboptimal.

As mentioned in section 2, our proposed implicit Rayleigh damping as an adjustment step (9) in the split-explicit time integration is equivalent to adding two terms directly in the vertical momentum equation: an implicit Rayleigh damping term for  $w$  and an implicit vertical diffusion of  $w$  [see eq. (12)]. Thus, this damping layer could be actually be implemented without significant additional complication by evaluating these two terms as part of the  $w$  equation, accommodating the vertical diffusion term as part of the vertically implicit solution for the vertically propagating acoustic modes. With this approach, one would have the option of specifying different coefficients for the two damping terms for the purpose of further improving the overall per-

formance of the absorbing layer. In practice, we have not found any systematic benefit in specifying different coefficients for these two damping terms, even though one (the Rayleigh damping) acts more selectively at relatively smaller scales and the other (vertical diffusion) at larger scales. This conclusion is based on recomputing the reflection coefficients in Fig. 12 with differing coefficients for the two damping terms (not shown), which is easily accommodated in the integration of (19). For  $\alpha = 0.1$  (Fig. 12a), choosing  $R_w/N = 5$  for the Rayleigh damping term and  $R_w/N = 20$  for the vertical diffusion term produced about the best result. However, in comparison to result with  $R_w/N = 10$  for both terms, the results are ambiguous; the reflection coefficient was somewhat lower for horizontal scales less than 40 km, somewhat higher for scales between 40 and 140 km, and about the same for scales larger than 140 km. For waves that are not as well resolved in the horizontal ( $\alpha = 0.3$  in Fig. 12b and  $\alpha = 0.5$  in Fig. 12c) the “best” values of  $R_w/N$  at both large and small scales are similar, suggesting that differing coefficients would not be of much benefit. However, whether or not differing coefficients are used, the numerical computation of these two terms as part of the vertical momentum equation could be beneficial in implementing this absorbing layer for other non-timesplit integration schemes (such as semi-implicit) in which an adjustment step as in (9) might not be applicable.

Although these results provide some general guidance for configuring the absorbing layer, for practical applications, particularly for ones in which there may be significant wave amplitude over a range of horizontal wavelengths, we would recommend some experimentation with the depth of the absorbing layer, vertical resolution within the layer, and variations in  $R_w$  to refine the coefficients suggested in Fig. 12. This implicit Rayleigh absorbing layer is included in the WRF/ARW community release, beginning with version V3.0.

*Acknowledgments.* We thank Bill Skamarock for his helpful suggestions on this work and Yaga Richter for facilitating this collaboration. We also thank Wei Wang for conducting the retrospective forecasts presented in section 6.

## APPENDIX

### Linear wave equation in the mass coordinate

To document the behavior of implicit Rayleigh damping on  $w$  in the mass-coordinate system, we shall simplify the equations by considering the linear equations under the same assumptions as in the linear analysis of the height-coordinate equations in section 3. For this purpose, we express the terrain-following vertical coordinate in

terms of mean-state quantities [ $\eta = (p_h - p_{ht})/\bar{\mu}$ ], where  $p_h$  is the hydrostatic pressure,  $\bar{\mu} = \bar{p}_{hs} - \bar{p}_{ht}$ , and subscripts  $s$  and  $t$  refer to the surface and the top of the model domain, respectively. Thus,  $\eta$  essentially reverts to the hydrostatic pressure vertical coordinate in this linear system. Adapting the linear mass-coordinate equations from the Appendix of Klemp et al. (2007) for the conditions considered in section 3, the small-time-step equations that include the implicit Rayleigh damping adjustment step are written as

$$u'^{\tau+\Delta\tau} = u'^{\tau} - \Delta\tau \left( \bar{\alpha} \partial_x p'^{\tau} + \partial_x \phi'^{\tau} + U \partial_x u'^{\tau} - f v'^{\tau} \right), \quad (\text{A1})$$

$$\partial_{\eta} \eta'^{\tau+\Delta\tau} = -\partial_x u'^{\tau+\Delta\tau}, \quad (\text{A2})$$

$$\theta'^{\tau+\Delta\tau} = \theta'^{\tau} - \Delta\tau \left( \bar{\theta}_{\eta} \eta'^{\tau+\Delta\tau} + U \partial_x \theta'^{\tau} \right), \quad (\text{A3})$$

$$\phi'_1 = \phi'^{\tau} - \Delta\tau \left( \bar{\phi}_{\eta} \eta'^{\tau+\Delta\tau} - \frac{1}{2} g w^{\tau} + U \partial_x \phi'^{\tau} \right), \quad (\text{A4})$$

$$w^{\tau*} = w^{\tau} + \Delta\tau \left( \frac{g}{\bar{\mu}} \bar{\partial}_{\eta} p'^{\tau*} - U \partial_x w^{\tau} \right), \quad (\text{A5})$$

$$\bar{p}^{\tau*} = \frac{c^2}{\bar{\alpha}} \left( \frac{\bar{\theta}^{\tau}}{\bar{\theta}} + \frac{1}{\bar{\mu}\bar{\alpha}} \bar{\partial}_{\eta} \phi'^{\tau*} \right) \quad (\text{A6})$$

$$\phi'^{\tau*} = \phi'_1 + \frac{1}{2} g \Delta\tau w^{\tau*}, \quad (\text{A7})$$

$$\boxed{w^{\tau+\Delta\tau} = w^{\tau*} - R_w \Delta\tau w^{\tau+\Delta\tau}} \quad (\text{A8})$$

$$\phi'^{\tau+\Delta\tau} = \phi'_1 + \frac{1}{2} g \Delta\tau w^{\tau+\Delta\tau}, \quad (\text{A9})$$

where  $\phi = \bar{\phi} + \phi'$  is the geopotential,  $\bar{\alpha}$  refers to the mean specific volume, and the boxed equation (A8) is the Rayleigh adjustment step for  $w$ . Here, (A6) represents the linear ideal gas law combined with the hydrostatic pressure relationship. Terms evaluated on the large time steps are denoted with the superscript  $t$ . Notice that for this simplified equation set the transverse velocity  $v'$  is integrated on the large time steps.

The procedure for advancing the small-time-step equations forward in time proceeds in the order of equations (A1)-(A9). Knowing all of the variables at time  $\tau$ :  $u'^{\tau+\Delta\tau}$  is obtained from (A1);  $\eta'^{\tau+\Delta\tau}$  is determined from the vertical integration of (A2);  $\theta'^{\tau+\Delta\tau}$  is computed from (A3); the known portion  $\phi'_1$  of the geopotential equation is computed using (A4);  $w^{\tau*}$  is recovered from the solution of a tridiagonal matrix formed by combining the vertical velocity equation (A5), the gas law and hydrostatic equation (A6), and the geopotential equation (A7); the implicit Rayleigh damping is applied in the adjustment step (A8); and  $\phi'^{\tau+\Delta\tau}$  is updated from (A9). At the end of the time step,  $p'^{\tau+\Delta\tau}$  is recovered by evaluating (A6) at the new time level.

As in the height-coordinate system, including the Rayleigh damping on  $w$  as an adjustment step is equivalent to a Rayleigh damping term inserted directly in the  $w$  equation plus an additional term containing a second derivative in the vertical. This is apparent in combining (A5)-(A9) to form a single equation for the full small time step for  $w$ :

$$\partial_\tau w - \frac{g}{\bar{\mu}} \overline{\partial_\eta p'^\tau} + R_w w^{\tau+\Delta\tau} - \frac{g^2 \Delta\tau^2}{4\bar{\mu}^2} \partial_\eta \left[ \frac{c^2}{\bar{\alpha}^2} \partial_\eta (R_w w^{\tau+\Delta\tau}) \right] = -U \partial_x w^t. \quad (\text{A10})$$

To document the behavior of our Rayleigh damping layer in the mass-coordinate equations for the steady linear mountain wave considered in section 3 (for the height coordinate), we write the steady state form of (A1)-(A9), using (A10) to represent the equivalent  $w$  equation for the full time step. Using the same assumptions of small Mach number and shallow atmosphere as in section 3, the 2D steady linear equations can be expressed as

$$U \partial_x u' + \partial_x \tilde{p}' + \partial_x \phi' - f v' = 0, \quad (\text{A11})$$

$$U \partial_x v' + f u' = 0 \quad (\text{A12})$$

$$U \partial_x w - \frac{g}{\bar{\mu} \bar{\alpha}} \partial_\eta \tilde{p}' + R_w w - \frac{c^2 \Delta\tau^2}{4} \frac{g}{\bar{\mu} \bar{\alpha}} \partial_\eta \left[ \frac{g}{\bar{\mu} \bar{\alpha}} \partial_\eta (R_w w) \right] = 0, \quad (\text{A13})$$

$$U \partial_x \tilde{\theta}' - \frac{N^2}{g^2} \tilde{\eta}' = 0, \quad (\text{A14})$$

$$\tilde{\eta}' + g w = 0, \quad (\text{A15})$$

$$\partial_x u' + \frac{1}{\bar{\mu} \bar{\alpha}} \partial_\eta \tilde{\eta}' = 0, \quad (\text{A16})$$

$$\tilde{\theta}' + \frac{1}{\bar{\mu} \bar{\alpha}} \partial_\eta \phi' = 0 \quad (\text{A17})$$

Following Klemp et al (2007), the perturbation variables have been scaled by defining  $\tilde{p}' = \bar{\alpha} p'$ ,  $\tilde{\eta}' = \bar{\mu} \bar{\alpha} \eta'$ ,  $\tilde{\theta}' = \theta'/\theta$ , and  $\tilde{\alpha}' = \alpha'/\bar{\alpha}$ . Writing the dependent variables  $\psi$  in terms of their Fourier components  $\psi = \hat{\psi} \exp(ikx)$  and recognizing that  $(g/\bar{\mu} \bar{\alpha}) \partial_\eta = -\partial_z$ , (A11)-(A17) can be combined into a single equation for  $\hat{w}$  that is identical to the wave equation (19) derived for the height-coordinate system. Thus, the implicit Rayleigh damping on  $w$ , applied as an adjustment at the end of the small time step in a split-explicit integration, has the same damping characteristics in both the height and mass coordinate equation sets.

## REFERENCES

Bougeault, P. and P. Mascart, eds., 2001: The Meso-NH Atmospheric Simulation System: Scientific Documentation. Météo France and

C.N.R.S., 337 pp. [at <http://mesonh.aero.obs-mip.fr/mesonh>]

Bougeault, P., 1983: A non-reflective upper boundary condition for limited-height hydrostatic models. *Mon. Wea. Rev.*, **111**, 420-429

Chen, C. C., D. R. Durran, and G. J. Hakim, 2005: Mountain-wave momentum flux in an evolving synoptic-scale flow. *J. Atmos. Sci.*, **62**, 3213-3231.

Doyle, J. D., M. A. Shapiro, Q. Jiang, and D. L. Bartels, 2005: Large-amplitude mountain wave breaking over Greenland. *J. Atmos. Sci.*, **62**, 3106-3126.

Durran, D. R., and J. B. Klemp, 1983: A compressible model for the simulation of moist mountain waves. *Mon. Wea. Rev.*, **111**, 2341-2361.

Grell, G. A., J. Dudhia, and D. R. Stauffer, 1995: A description of the fifth-generation Penn State/NCAR Mesoscale Model (MM5). *NCAR Technical Note*, NCAR/TN-398 + STR, 122 pp. [at <http://www.mmm.ucar.edu/mm5/documents/mm5-desc-doc.html>]

Hahn, D., 2007: Evaluation of WRF performance for depicting orographically-induced gravity waves in the stratosphere. *Eighth WRF Users Workshop*, Boulder, CO, June 2007. [at [http://www.mmm.ucar.edu/wrf/users/workshops/WS2007/abstracts/2-6\\_Hahn.pdf](http://www.mmm.ucar.edu/wrf/users/workshops/WS2007/abstracts/2-6_Hahn.pdf)]

Jiang, Q., and J. D. Doyle, 2004: Gravity wave breaking over the central Alps: role of complex terrain. *J. Atmos. Sci.*, **61**, 2249-2266.

Klemp, J. B., and D. R. Durran. 1983: An upper boundary condition permitting internal gravity wave radiation in numerical mesoscale models. *Mon. Wea. Rev.*, **111**, 430-444.

Klemp, J. B., and D. K. Lilly, 1978: Numerical simulation of hydrostatic mountain waves. *J. Atmos. Sci.*, **35**, 78-107.

Klemp, J. B., and D. K. Lilly, 1980: Mountain waves and momentum flux. *Orographic Effects in Planetary Flows*, GARP Publication series No. 23, ICSU/WMO, Geneva, 116-141.

Klemp, J. B., W. C. Skamarock, and J. Dudhia, 2007: Conservative split-explicit time integration methods for the compressible nonhydrostatic equations. *Mon. Wea. Rev.*, **135**, 2897-2913.

Mission Research Corporation/ASTER Division, 2000: RAMS. The Regional Atmospheric Modeling System. Technical Description., 50 pp. [at [http://www.atmet.com/html/docs/rams/rams\\_tech.pdf](http://www.atmet.com/html/docs/rams/rams_tech.pdf)]

Rotunno, R., J. B. Klemp, and M. L. Weisman, 1988: A theory for long-lived squall lines. *J. Atmos. Sci.*, **45**, 463-485.

Skamarock, W. C., J. B. Klemp, J. Dudhia, D. O. Gill, D. M. Barker, W. Wang, J. G. Powers,

- 2005: A description of the Advanced Research WRF Version 2. *NCAR Tech. Note*, ncar/TN-468+STR, 88 pp.
- Skamarock, W. C., and J. B. Klemp, 2007: A time-split nonhydrostatic atmospheric model for weather research and forecasting applications. *J. Comp. Phys.*, **227**, 3465-3485.
- Smith, R. B., 1979: The influence of mountains on the atmosphere. B. Saltzman, Ed., *Adv. Geophys.*, **21**, 87-230.
- Wei, H., D. H. Bromwich, L.-S. Bai, Y.-H. Kuo, and T. K. Wee, 2002: A case study of upper boundary condition in MM5 over Antarctica. *Twelfth PSU/NCAR Mesoscale Model Users Workshop*, Boulder, CO, June, 2002. [at [www.mmm.ucar.edu/mm5/workshop/ws02/Wei.pdf](http://www.mmm.ucar.edu/mm5/workshop/ws02/Wei.pdf)]
- Weisman, M. L., and J. B. Klemp, 1982: The dependence of convective storms on vertical wind shear and buoyancy. *Mon. Wea. Rev.*, **110**, 50-66.
- Weisman, M. L., J. B. Klemp and R. Rotunno, 1988: The structure and evolution of numerically simulated squall lines. *J. Atmos. Sci.*, **45**, 1990-2013.
- Xue, M., K. K. Droegemeier, V. Wong, A. Shapiro, and K. Brewster, 1995: ARPS Version 4.0 Users Guide. Center for the Analysis and Prediction of Storms, University of Oklahoma, 380 pp. [at <http://www.caps.ou.edu/ARPS/arpdoc.html>]
- Zängl, G., 2007: An adaptive vertical coordinate formulation for a nonhydrostatic model with flux-form equations. *Mon. Wea. Rev.*, **135**, 228-239.